Letter

Barkhausen noise from formation of 360° domain walls in disordered permalloy thin films

Sami Kaappa and Lasse Laurson
Computational Physics Laboratory, Tampere University, P.O. Box 692, FI-33014 Tampere, Finland

(Received 23 June 2022; revised 28 February 2023; accepted 2 March 2023; published 6 April 2023)

Barkhausen noise in disordered ferromagnets is typically understood to originate primarily from jerky field-driven motion of domain walls. We study the magnetization reversal process in disordered permalloy thin films using micromagnetic simulations and find that the magnetization reversal process consists of gradual formation of immobile 360° domain walls via a sequence of localized magnetization rotation events. The density of 360° domain walls formed within the sample as well as the statistical properties of the Barkhausen jumps are controlled by the disorder strength.

DOI: 10.1103/PhysRevResearch.5.L022006

I. INTRODUCTION

Permalloy ($Ni_{80}Fe_{20}$, Py) thin films are important ferromagnetic systems in spintronics and magnonics applications [1–5] due to their soft magnetic response and low fabrication cost. Py thin films exhibit a hysteretic response to external fields and display crackling noise [6–8] known as Barkhausen noise (BN) [9]. The statistical properties of BN are typically found to obey power law behavior [9–11]. Statistical physicists often model BN by employing either so-called front propagation or nucleation models, such as the random-field Ising model (RFIM) [6–8,12–18], with the BN in the neighborhood of the coercive field (where the largest BN amplitude is found) understood to originate from the jerky field-driven motion of domain walls (DWs). However, given the vanishing magnetocrystalline anisotropy of Py, Ising-type models which inherently assume a strong uniaxial anisotropy are not suitable to properly characterize its magnetization reversal process.

In this work, we employ full micromagnetic simulations of disordered Py thin films to properly capture the details of the field-driven magnetization reversal process and the related statistical properties, including the emergence of BN. Unlike simple Ising-type models, micromagnetic simulations provide a proper description of the full vectorial nature of the order parameter (magnetization) and include all the relevant energy terms (such as the demagnetizing energy). Contrary to the paradigm of BN due to jerky motion of DWs, we find that field-driven BN in Py thin films is due to the gradual formation of largely *immobile* 360° DWs [19–31] via a sequence of localized and intermittent magnetization rotation events. Once formed, the 360° DWs get progressively narrower due to an increasing driving field induced effective anisotropy, before disappearing as the oppositely saturated state is reached. Both the emerging configuration of 360° DWs (e.g., their density) and the statistics of BN are found to be dependent on disorder strength, suggesting that the magnetization reversal process in disordered Py thin films is governed by disorder-induced criticality [10], but with an important difference compared to Ising models: no infinite, spanning avalanche (i.e., an avalanche spanning the finite system along at least one of its dimensions, resulting in a jump of magnetization in an infinite system below the critical disorder) is observed for weak, subcritical disorder. The present work therefore focuses on investigating how the Barkhausen effect and the related jump size distributions emerge from the previously unidentified mechanism of gradual formation of immobile 360° domain walls in thin films with negligible magnetocrystalline anisotropy, as opposed to the well-known mechanism related to the jerky motion of domain walls.

II. COMPUTATIONAL METHODS

Our micromagnetic simulations are performed using the GPU-accelerated simulation code MUMAX3 [32]. Typically, micromagnetic simulations rely on the dynamical approach where the magnetization dynamics is governed by the Landau-Lifshitz-Gilbert equation, written as

$$\frac{\partial \vec{M}}{\partial t} = \frac{\gamma}{1+\alpha^2}[\vec{M} \times \vec{H}_{\text{eff}} + \alpha \vec{M} \times (\vec{M} \times \vec{H}_{\text{eff}})], \quad (1)$$

where $\vec{M} = M_s \hat{m}$ is the magnetization vector, M_s is the saturation magnetization, $\hat{m} = m_x \hat{x} + m_y \hat{y} + m_z \hat{z}$ is the unit vector pointing along the magnetization, γ is the gyromagnetic ratio of electron, α is the Gilbert damping constant, and $\vec{H}_{\text{eff}}$ is the effective field. The total energy of the system (and hence $\vec{H}_{\text{eff}}$) consists of contributions from exchange, demagnetization, and Zeeman terms as described in detail in the Supplemental Material [33]. Due to the vanishing magnetocrystalline anisotropy of Py, the anisotropy energy is neglected here; that is, the magnetocrystalline anisotropy constants are set to zero.

An example of a simulated system is shown in Fig. 1(a). We discretize the square thin film on a finite difference grid with spacing of 4 nm in the x and y in-plane directions where

Published by the American Physical Society under the terms of the Creative Commons Attribution 4.0 International license. Further distribution of this work must maintain attribution to the author(s) and the published article's title, journal citation, and DOI.

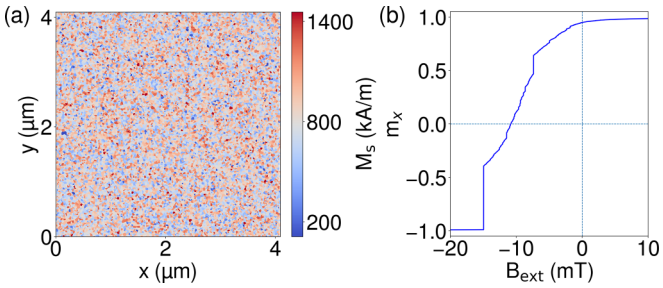

FIG. 1. (a) Example of the spatial variation of M_s, sampled from the normal distribution with mean 800 kA/m and standard deviation of 30% of the mean value. (b) Example evolution of m_x with quasistatically decreasing B_{ext}.

the linear system size is 4096 nm and consider a single 16 nm long cell in the perpendicular z direction (the film thickness). Periodic boundary conditions are employed in the in-plane x and y directions. We use the common literature values for the exchange stiffness $A = 13$ pJ/m and the average saturation magnetization $M_s = 800$ kA/m. Structural disorder is introduced via a spatially varying M_s by performing a two-dimensional (2D) Voronoi tessellation on each sample with the grain size of 30 nm (the disorder correlation length) and assigning a random value of M_s in each grain from a normal distribution with mean of 800 kA/m and standard deviations (the disorder strengths) between 5% and 35% of the mean value (negative M_s values are avoided by redrawing until a positive value is obtained) [34,35]. This way, we establish a random component in the energy landscape of the magnetization state, characterized by the correlation length (Voronoi grain size) and magnitude (disorder strength) of the disorder. In a material, such disorder can be caused by inhomogeneous distribution of elements in the sample, impurity material, defects, and other lattice imperfections. Introducing the disorder by parameter variation in the zero-anisotropy case can be done through variation of either M_s or A or both. Here we investigate the effect of the M_s variation only. According to our test runs, simultaneous variation of exchange stiffness A does not alter the magnetization dynamics qualitatively but the dynamical process is dominated by the spatial M_s variation.

In each run, the magnitude B_{ext} of the external field $\vec{B}_{\text{ext}} = B_{\text{ext}}\hat{x}$ is swept from 100 mT (at which point the system is close to saturation with $m_x \approx 1$) to -100 mT. The run is considered finished once m_x falls below -0.98 or the external field reaches -100 mT. This procedure thus produces half of the hysteresis loop where m_x reverses from a value close to $+1$ to a value close to -1.

The simulation times of dynamic simulations are in practice limited to the microsecond range, hence seriously limiting the range of accessible field frequencies. Therefore, we mainly focus on *quasistatic* simulations, where the total energy of the system is consecutively minimized while altering B_{ext} between each minimization in small steps ΔB_{ext}. To validate the use of quasistatic simulations, we present in the Supplemental Material [33] results for both dynamical and quasistatic simulations, showing how the dynamic hysteresis loops approach the hysteresis loop obtained from the quasistatic simulations in the low frequency limit of the sinusoidal driving field. In what follows, we thus consider quasistatic simulations with $|\Delta B_{\text{ext}}| = 4$ T; see the Supplemental Material [33] for the justification of the selected value. For an example of the half loop produced by this protocol, see Fig. 1(b). For each disorder strength, we collect statistics by running 40 simulation runs with different disorder realizations.

III. RESULTS AND DISCUSSION

A. Hysteresis curves

Figure 2 shows all of the simulated hysteresis curves for each disorder strength. The curves for 5 and 10% disorders are quite smooth, i.e., Barkhausen jumps are largely absent. The magnetization is being rotated in a smooth and continuous fashion as the applied field is driven from 100 mT to -100 mT, i.e., no infinite spanning avalanche takes place unlike in RFIM for weak disorder. Note also that the magnetization does not saturate to -1 before $B_{\text{ext}} = -30$ mT. In contrast, the systems with the highest disorder strengths, 30% and 35%, exhibit bursty behavior with more frequent and larger abrupt avalanches. The saturated state with $m_x = -1$ is reached before $B_{\text{ext}} = -30$ mT for most runs. The curves with 20% disorder show features of both kinds: long smooth sections interrupted by occasional abrupt jumps.

Following this observation, let us make a distinction between the parts of the hysteresis curve where (1) the magnetization is rotated smoothly and continuously and (2) a large part of the magnetization is changed abruptly (Barkhausen jumps). We note that the tangential slopes of the smooth parts in between avalanches seem to have a characteristic magnitude. Also, the curves with 10 and 20% disorder strengths seem to be divided into two separate subgroups, as well as the 30% curves into four subgroups (Fig. 2). In the following, we will connect all of these features of the hysteresis curves to the disorder strength, the respective Barkhausen jump size distributions, and the magnetization reversal mechanisms, including the appearance of the 360° DWs.

B. Barkhausen jump size distributions

Figure 3 shows the Barkhausen jump size distributions—that is, the distributions of the absolute changes $s \equiv |\Delta m_x|$ of m_x during each field step in the quasistatic simulations. Based on the renormalization group theory and previous studies of Barkhausen noise statistics [9], we expect that the tails of size distributions $P(s)$ follow truncated power laws with a critical exponent τ,

$$P(s) = s^{-\tau} g(s/s_0), \tag{2}$$

where $g(x)$ is a cutoff scaling function and s_0 a cutoff scale parameter. The tails of the distributions in Fig. 3 do behave according to Eq. (2) with a disorder-dependent s_0 (see below for more details), but a bump exists in each distribution below the power-law part, introducing a characteristic length scale to the statistics. Increasing the disorder strength leads to translation of the bump to smaller jump sizes and possibly to broadening of the bump. We attribute the positions of the bumps to the largest magnitudes for the tangential slopes in the hysteresis curves where the magnetization reversal is

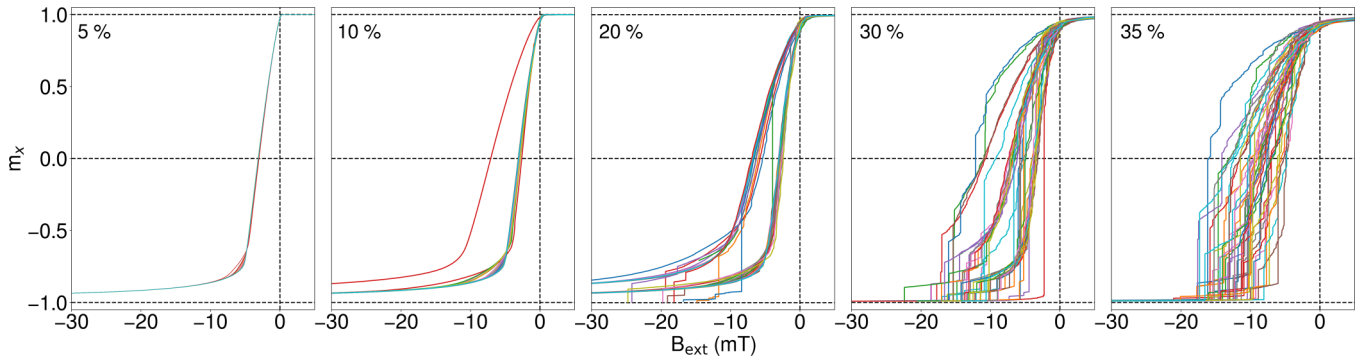

FIG. 2. Hysteresis curves for $m_x(B_{\text{ext}})$ of all simulations. The external field B_{ext} is decreased from 100 mT to −100 mT. The disorder strength is indicated in the upper left corner of each panel.

smooth. Avalanches exceeding the characteristic size of the bumps, obeying Eq. (2), are taken to be the actual Barkhausen jumps.

The disorder strength of 35% seems to be close to the critical disorder strength since the tail of $P(s)$ exhibits a clear power law behavior. Even though the expected shape of Eq. (2) includes the cutoff function $g(x)$, we employed a plain power law fit with $g = 1$ in the absence of properly resolved cutoffs due to limited statistics. Fitting a power law to the tail of $P(s)$ for 35% disorder results in $\tau = 1.75 \pm 0.02$. As illustrated in the inset of Fig. 3, the distributions for the other disorder strengths fall off from the power law trend in the order given by the disorder strength, i.e., s_0 in Eq. (2) is disorder dependent. This trend is expected when approaching the critical disorder strength, and so we conclude that the critical disorder strength here is likely to be close to 35%. In the literature, the reported values for the critical exponent τ for Py thin films are diverse: 1.65 [6], 1.33 [8], 1.45 [16], and 1.6 [36]. Our estimate is close to those reported in Refs. [6] and [36].

Another interesting feature in the distributions is the almost perfect power law behavior for jump sizes smaller than that of the bumps of the 5–20% disorder distributions; this seems to be absent in the stronger disorder statistics. These very small magnetization changes correspond to tangential slopes of $m_x(B_{\text{ext}})$ smaller in magnitude than the ones of the bump and originate from the parts of the hysteresis curves where the magnetization is close to saturation. It is worth noting that the bump positions depend also somewhat on the field step used in the simulations; see the Supplemental Material [33].

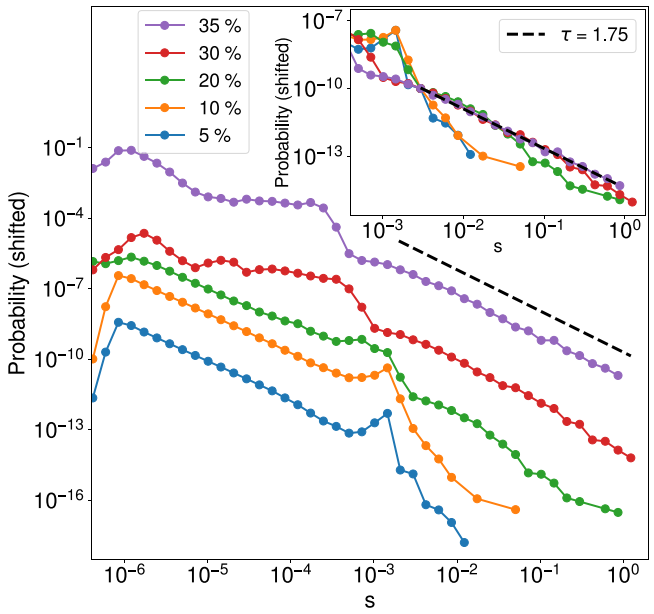

FIG. 3. Distributions (shifted vertically for clarity) of the Barkhausen jump sizes $s = |\Delta m_x|$ for different disorder strengths. The exponent $\tau = 1.75 \pm 0.02$ is determined by fitting a power law to the tail of the 35% distribution. The inset includes the same data stacked on top of each other to highlight the dependence of s_0 on the disorder strength.

C. Magnetization reversal processes

To understand the origin of the observed subgroups in the hysteresis curves we proceed to study the disorder-dependent magnetization reversal mechanisms. For 5% disorder [Fig. 4(a)], we observe that, interestingly, a structure of two 360° DWs is formed at the late stages of the reversal process. This formation process proceeds via a gradual rotation of the magnetization in opposite directions within two "domains," such that the eventual 360° DWs are formed via 90° DWs at $B_{\text{ext}} = -1.59$ mT and 180° DWs at $B_{\text{ext}} = 3.21$ mT. Due to topological protection [24], the 360° DWs remain in the system until the end of the simulation, resulting in the absence of full negative saturation of m_x for the B_{ext} values considered. Upon making B_{ext} more negative, m_x is slowly approaching −1 since the widths w of the DWs decrease with increase of the B_{ext} (see Fig. 5 and the related discussion below). Each of the runs with 5% disorder exhibits the formation of two 360° DWs and the hysteresis curves of the different realizations overlap almost perfectly (Fig. 2).

For 10 and 20% disorder, the two subgroups of the hysteresis curves in Fig. 2 correspond to two and four 360° DWs per simulation box, respectively, and some of the 360° DW structures disappear before the applied field reaches −25 mT; this is seen as m_x reaching −1 in Fig. 2. The reversal mechanism in an example run where four 360° DWs are formed is presented in Fig. 4(b). The mechanism for the formation of the DWs is similar to that of the 5% disorder in Fig. 4(a), but there

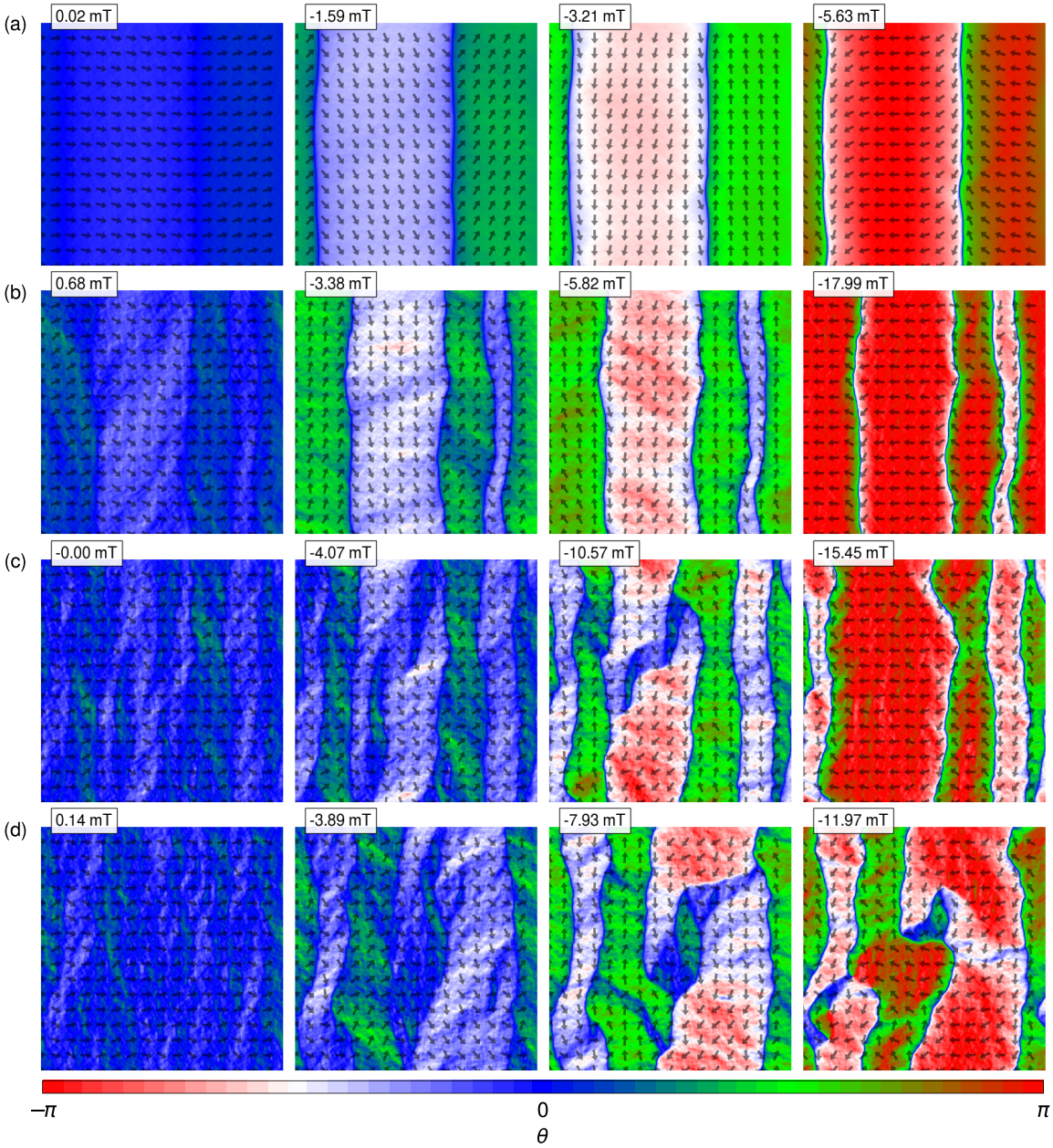

FIG. 4. Examples of the magnetization reversal mechanism with (a) 5%, (b) 20%, (c) 30%, and (d) 35% disorder strengths. The arrows denote the local magnetization direction in every 64th grid point. The background color indicates the direction of the local magnetization $\vec{m}$ as given by the color bar; θ denotes the angle between the x axis and $\vec{m}$ in radians. The B_{ext} values corresponding to each snapshot are indicated in the top left corners.

is more spatial variation in the local magnetization and the DWs appear more rough. As expected, even more roughness is present in the example cases with 30 and 35% disorders shown in Figs. 4(c) and 4(d), where the final magnetization structures are more complicated and features resembling 360° DWs can be recognized only in parts of the system. The magnetization configurations shown in both Figs. 4(c) and 4(d) are fully reversed towards the field direction at the next field step. A closer look at the 30% disorder strength hysteresis curves in Fig. 2 reveals that there are distinct subgroups of curves that correspond to a varying number of DWs (up to 6 or 8) in the system. Four example runs with 30% disorder are highlighted in the Supplemental Material [33], further illustrating the different magnetization reversal mechanisms involving formation of different numbers of DWs. With the highest disorder strengths of 30 and 35%, the unambiguous 360° DWs are reached only in the late stage of the runs if at all. Animations of the magnetization reversal processes for different disorder strengths are provided as Supplemental Material [33]. We ruled out the possibility of 360° DWs forming due to periodic boundary conditions by a similar calculation with open boundaries as presented in the Supplemental Material [33].

Thus stronger disorder induces the formation of a higher density of 360° DWs that also appear less stable—presumably disorder lowers the energy barrier to remove a 360° DW,

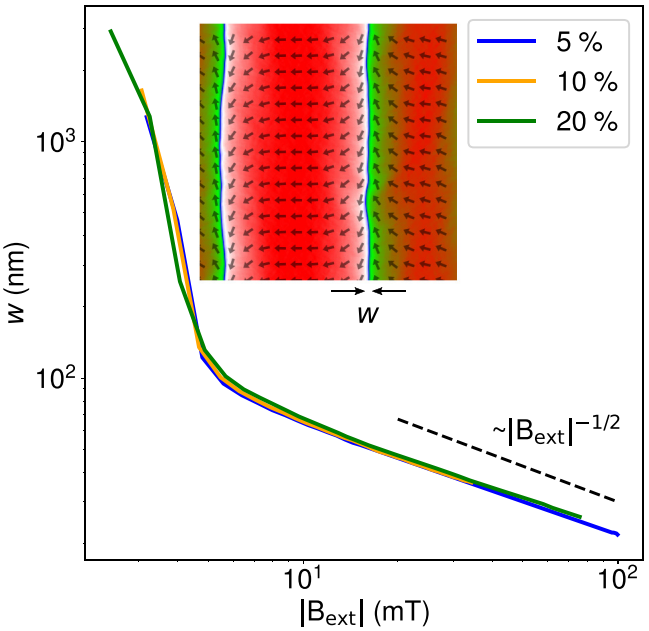

FIG. 5. 360° DW width w as a function of $|B_{\text{ext}}|$ in selected runs with varying disorder strength where two 360° DWs are formed. w evolves approximately as $|B_{\text{ext}}|^{-1/2}$ (dashed line). The inset shows an example configuration where w is evaluated at $B_{\text{ext}} = -5.6$ mT for 5% disorder. w is taken to be the distance between the two points at which the magnetization profile $m_x(x)$, averaged over y, crosses zero.

thus rendering the topological protection less effective. For example, in the case of 30% disorder, all the hysteresis curves collapse to -1 before B_{ext} has reached -25 mT. Before collapsing, the DW width w behaves like $w \sim |B_{\text{ext}}|^{-1/2}$, as demonstrated in Fig. 5. The inverse square root relation between w and the uniaxial anisotropy constant is a well-known result [37] for stationary 180° DWs and our numerical examination verifies that B_{ext} affects the immobile 360° DWs in a similar way as the uniaxial magnetocrystalline anisotropy affects 180° DWs. The disorder strength does not seem to affect the $w(|B_{\text{ext}}|)$ relation.

IV. CONCLUSIONS

To conclude, our full micromagnetic simulations suggest that Barkhausen noise in Py thin films obeys neither predictions of nucleation nor front propagation models, but is instead a consequence of gradual formation of immobile 360° DWs via a sequence of abrupt magnetization rotation events. The criticality exhibited by the system appears to be disorder induced such that the cutoff avalanche size is disorder dependent. However, the "infinite avalanche" typically observed in Ising-type models for weak disorder is absent here. Instead, we observe smooth hysteresis curves for weak disorder, with progressively larger Barkhausen jumps as disorder is made stronger so that the critical disorder strength is approached from below. Disorder also controls the morphology of the ensuing 360° DWs such that for weak disorder almost straight DWs spanning the system are formed. Upon increasing the disorder strength, the DWs become increasingly rough and finally form an irregular DW structure without clear, spanning 360° DWs at the critical disorder strength. The property of the Py samples not having any magnetocrystalline anisotropy results in the magnetization reversal process happening in a sequence of gradual and localized rotations of the magnetization, highlighting the importance of using full micromagnetic simulations to properly capture the details of the magnetization reversal process [38] and calling for experimental verification of our results, e.g., using magneto-optical imaging [39,40].

ACKNOWLEDGMENTS

The authors acknowledge the computational resources provided by CSC and support of the Academy of Finland via the Academy Project BarFume (Project No. 338955).

[1] S. Gardelis, C. G. Smith, C. H. W. Barnes, E. H. Linfield, and D. A. Ritchie, Spin-valve effects in a semiconductor field-effect transistor: A spintronic device, Phys. Rev. B **60**, 7764 (1999).

[2] F. J. Jedema, A. T. Filip, and B. J. van Wees, Electrical spin injection and accumulation at room temperature in an all-metal mesoscopic spin valve, Nature (London) **410**, 345 (2001).

[3] B. F. Miao, S. Y. Huang, D. Qu, and C. L. Chien, Inverse Spin Hall Effect in a Ferromagnetic Metal, Phys. Rev. Lett. **111**, 066602 (2013).

[4] M. Haidar, A. A. Awad, M. Dvornik, R. Khymyn, A. Houshang, and J. Åkerman, A single layer spin-orbit torque nano-oscillator, Nat. Commun. **10**, 2362 (2019).

[5] S. P. Bommanaboyena, D. Backes, L. S. I. Veiga, S. S. Dhesi, Y. R. Niu, B. Sarpi, T. Denneulin, A. Kovács, T. Mashoff, O. Gomonay, J. Sinova, K. Everschor-Sitte, D. Schönke, R. M. Reeve, M. Kläui, H.-J. Elmers, and M. Jourdan, Readout of an antiferromagnetic spintronics system by strong exchange coupling of Mn_2Au and permalloy, Nat. Commun. **12**, 6539 (2021).

[6] A. Roy and P. S. A. Kumar, Breakdown of Barkhausen criticality in an ultrathin ferromagnetic film, J. Supercond. Novel Magn. **33**, 2773 (2020).

[7] A. Roy and P. S. A. Kumar, A study of Barkhausen avalanche statistics through the critical disorder in a ferromagnetic thin film: Experimental investigation and theoretical modeling, J. Magn. Magn. Mater. **493**, 165710 (2020).

[8] S. Yang and J. L. Erskine, Domain wall dynamics and Barkhausen jumps in thin-film permalloy microstructures, Phys. Rev. B **72**, 064433 (2005).

[9] G. Durin and S. Zapperi, The Barkhausen effect, in *The Science of Hysteresis*, edited by G. Bertotti and I. Mayergoyz (Academic Press, Amsterdam, 2006), Chap. 3, pp. 181–267.

[10] J. P. Sethna, K. A. Dahmen, and C. R. Myers, Crackling noise, Nature (London) **410**, 242 (2001).

[11] S. Zapperi, P. Cizeau, G. Durin, and H. E. Stanley, Dynamics of a ferromagnetic domain wall: Avalanches, depinning transition, and the Barkhausen effect, Phys. Rev. B **58**, 6353 (1998).

[12] E. Puppin, S. Ricci, and L. Callegaro, Barkhausen jumps in a magnetic microstructure, Appl. Phys. Lett. **76**, 2418 (2000).

[13] D.-H. Kim, S.-B. Choe, and S.-C. Shin, Direct Observation of Barkhausen Avalanche in Co Thin Films, Phys. Rev. Lett. **90**, 087203 (2003).

[14] M. Zani and E. Puppin, Temperature dependent criticality of Barkhausen noise in thin Fe films, J. Magn. Magn. Mater. **272**, E865 (2004).

[15] L. Santi, F. Bohn, A. D. C. Viegas, G. Durin, A. Magni, R. Bonin, S. Zapperi, and R. L. Sommer, Effects of thickness on the statistical properties of the Barkhausen noise in amorphous films, Phys. B: Condens. Matter **384**, 144 (2006).

[16] S. Yang, G. S. D. Beach, and J. L. Erskine, Negative Barkhausen jumps in permalloy thin-film microstructures, J. Appl. Phys. **100**, 113914 (2006).

[17] S. Janićević, D. Jovković, L. Laurson, and D. Spasojević, Threshold-induced correlations in the Random Field Ising Model, Sci. Rep. **8**, 2571 (2018).

[18] A. Mughal, L. Laurson, G. Durin, and S. Zapperi, Effect of dipolar interactions for domain-wall dynamics in magnetic thin films, IEEE Trans. Magn. **46**, 228 (2010).

[19] D. O. Smith and K. J. Harte, Noncoherent switching in permalloy films, J. Appl. Phys. **33**, 1399 (1962).

[20] H. S. Cho, C. Hou, M. Sun, and H. Fujiwara, Characteristics of 360°-domain walls observed by magnetic force microscope in exchange-biased NiFe films, J. Appl. Phys. **85**, 5160 (1999).

[21] W. H. Rippard, A. C. Perrella, P. Chalsani, F. J. Albert, J. A. Katine, and R. A. Buhrman, Observation of magnetization reversal of thin-film permalloy nanostructures using ballistic electron magnetic microscopy, Appl. Phys. Lett. **77**, 1357 (2000).

[22] F. J. Castano, C. A. Ross, C. Frandsen, A. Eilez, D. Gil, H. I. Smith, M. Redjdal, and F. B. Humphrey, Metastable states in magnetic nanorings, Phys. Rev. B **67**, 184425 (2003).

[23] M. Hehn, D. Lacour, F. Montaigne, J. Briones, R. Belkhou, S. E. Moussaoui, F. Maccherozzi, and N. Rougemaille, 360° domain wall generation in the soft layer of magnetic tunnel junctions, Appl. Phys. Lett. **92**, 072501 (2008).

[24] J. Zhang, S. A. Siddiqui, P. Ho, J. A. Currivan-Incorvia, L. Tryputen, E. Lage, D. C. Bono, M. A. Baldo, and C. A. Ross, 360° domain walls: Stability, magnetic field and electric current effects, New J. Phys. **18**, 053028 (2016).

[25] M. O. Liedke, K. Potzger, A. H. Bothmer, J. Fassbender, B. Hillebrands, M. Rickart, and P. P. Freitas, Domain structure during magnetization reversal of PtMn CoFe exchange bias micropatterned lines, J. Appl. Phys. **100**, 043918 (2006).

[26] K. J. O'Shea, K. Rode, H. Kurt, D. McGrouther, and D. A. MacLaren, Concentric 360° domain wall nesting in magnetic tunnel junction films: A Lorentz TEM study, J. Phys. D **48**, 055001 (2015).

[27] N. Chowdhury, W. Kleemann, O. Petracic, F. Kronast, A. Doran, A. Scholl, S. Cardoso, P. Freitas, and S. Bedanta, 360° domain walls in magnetic thin films with uniaxial and random anisotropy, Phys. Rev. B **98**, 134440 (2018).

[28] C. B. Muratov and V. V. Osipov, Theory of 360° domain walls in thin ferromagnetic films, J. Appl. Phys. **104**, 053908 (2008).

[29] J. Dean, A. Kohn, A. Kovács, A. Zeltser, M. J. Carey, G. Hrkac, D. A. Allwood, and T. Schrefl, The formation mechanism of 360° domain walls in exchange-biased polycrystalline ferromagnetic films, J. Appl. Phys. **110**, 073901 (2011).

[30] Y. Su, L. Weng, W. Dong, B. Xi, R. Xiong, and J. Hu, Remarkably enhanced current-driven 360° domain wall motion in nanostripe by tuning in-plane biaxial anisotropy, Sci. Rep. **7**, 13416 (2017).

[31] M. Li and J. Lu, Survey of 360° domain walls in magnetic heterostructures: Topology, chirality and current-driven dynamics, J. Magn. Magn. Mater. **525**, 167684 (2021).

[32] A. Vansteenkiste, J. Leliaert, M. Dvornik, M. Helsen, F. Garcia-Sanchez, and B. V. Waeyenberge, The design and verification of MuMax3, AIP Adv. **4**, 107133 (2014).

[33] See Supplemental Material at http://link.aps.org/supplemental/10.1103/PhysRevResearch.5.L022006 for additional information on the expression for the effective field, justification of the quasistatic simulations, the field step, and the magnetization reversal processes in systems with 30% disorder, as well as for movies of selected magnetization reversal processes.

[34] H. Min, R. D. McMichael, M. J. Donahue, J. Miltat, and M. D. Stiles, Effects of Disorder and Internal Dynamics on Vortex Wall Propagation, Phys. Rev. Lett. **104**, 217201 (2010).

[35] J. Leliaert, B. V. D. Wiele, A. Vansteenkiste, L. Laurson, G. Durin, L. Dupré, and B. V. Waeyenberge, A numerical approach to incorporate intrinsic material defects in micromagnetic simulations, J. Appl. Phys. **115**, 17D102 (2014).

[36] N. J. Wiegman, Barkhausen noise in magnetic thin films, Doctoral dissertation, Technische Hogeschool Eindhoven, 1979.

[37] S. Chikazumi and C. D. Graham, *Physics of Ferromagnetism*, International Series of Monographs on Physics (Oxford University Press, Oxford, 1997).

[38] T. Herranen and L. Laurson, Barkhausen Noise from Precessional Domain Wall Motion, Phys. Rev. Lett. **122**, 117205 (2019).

[39] R. Schäfer, Investigation of domains and dynamics of domain walls by the magneto-optical kerr-effect, in *Handbook of Magnetism and Advanced Magnetic Materials*, edited by H. Kronmüller, S. Parkin, R. Wiesendanger, and G. Guntherodt (Wiley, New York, 2007).

[40] J. Dormand and P. Prince, A family of embedded Runge-Kutta formulae, J. Comput. Appl. Math. **6**, 19 (1980).